Numerical Investigation of Tear Testing of a Single Weld Formed by Fused Filament Fabrication☆

Zheliang Wang[a], Ojaswi Agarwal[a], Jonathan E. Seppala[c], Kevin J. Hemker[a], Thao D. Nguyen[a,b,*]

[a]*Department of Mechanical Engineering, The Johns Hopkins University, Baltimore, MD 21218, USA*
[b]*Department of Materials Science and Engineering, The Johns Hopkins University, Baltimore, MD 21218, USA*
[c]*Materials Science and Engineering Division, National Institute of Standards and Technology, Gaithersburg, MD 20899, USA*

Abstract

The tear test is widely used to measure the fracture toughness of thin rubbers sheets and polymer films. More recently, the tear test has been applied to polymer materials produced by melt extrusion additive manufacturing to measure the fracture toughness of a single weld between two printed (extruded) filaments. This paper presents a finite element modeling study of the tearing of a weld between two printed filaments to investigate the mechanics of the tear test and the effects of geometry and material properties on the tear energy. The mechanical behavior of the printed filaments was described by a viscoplastic model for glassy polymers and the weld was represented using cohesive surface elements and the Xu-Needleman traction-separation relationship. The geometric model and the material parameters were chosen based on the experimental measurements. The tear energy varied with the specimen dimensions, curvature of the printed filaments, the yield stress relative to the cohesive strength of the weld, and the post-yield stress drop. The effects of the hardening modulus was small. These factors altered the viscoplastic dissipation in the material ahead of the propagating crack tip. The results showed that viscoplastic dissipation constitutes a large fraction of the tear energy and is strongly affected by the specimen dimensions and the geometry and material properties of the printed filament. There was also considerable mode mixty in the tear energy. The findings can be used to design tear tests to measure the intrinsic fracture toughness of the weld.

Keywords: trouser tear test, 3D printing, finite element simulation, stick-slip

1. Introduction

The tear test, also referred to as the trouser tear test, was first proposed by Rivlin and Thomas [1] to measure a material property, termed the tear energy, to describe the failure behavior of vulcanized rubber sheets. In a tear test, a notch is created along the centerline of a rectangular specimen to create two tear arms, which are pulled in the opposite direction perpendicular to the sheet to propagate the tear. The tear test has the advantage that the tear energy can be evaluated analytically from the measured tear force, the thickness and width of the sheet, and the elastic properties of the sheet assuming negligible inelastic deformation [1]. Since its introduction, the tear test has become a standard test for measuring the failure properties of elastomeric sheets (ASTM-D624 [2]) and polymer films (ASTM D-1938 [3]). The tear test has also been applied to other materials including metals [4, 5] and biomaterials [6, 7, 8].

More recently, the tear the test has been applied to study the failure of a single weld produced by fused filament fabrication (FFF), a melt extrusion polymer additive manufacturing method [9]. In FFF, a thermoplastic material, such as polycarbonate, is heated to above the glass transition temperature T_g to produce a melt, which is then extruded through a nozzle, and deposited layer by layer to create a part. Printing a filament locally heats the surrounding filaments to above the T_g allowing the polymer chains to inter-diffuse and weld the filaments together. Parts printed by

*Corresponding author
Email address: `Vicky.Nguyen@jhu.edu` (Thao D. Nguyen)

FFF suffer from lower strength and fracture toughness compared to the bulk materials and the failure typically starts at the welds [10, 11, 12, 13].

Seppala and coworkers [9, 14] applied the tear test to an FFF printed ABS wall to measure the tear energy of a single weld. The authors interpreted the tear energy as a Mode III fracture energy and showed that it increased with the effective welding time. The tear test has since become an increasingly popular method to characterize the failure property of the printed welds [15, 16, 17]. Many of these investigators have also interpreted the tear energy as the Mode III fracture energy. However, the mechanics of the tear test applied to a thick thermoplastic specimen is not well understood. We applied the tear test of an FFF printed polycarbonate wall to investigate the effect of printing conditions, such as the layer width and the printing temperature on the tear energy of the printed welds [18]. We observed that the unconstrained portion of the specimen ahead of the crack tip rotated during tearing. This suggests that the tear energy represents a mixed mode fracture energy rather than a Mode III fracture energy, and that the mode mixty changes with crack propagation because of the continued specimen rotation. The same phenomenon was reported by Bayart et al. [19] during tear testing of polypropylene thin films. However, the cause of the specimen rotation and the effects of the specimen geometry on the rotation have not been investigated. We also observed that the tear propagated in a discontinuous, stick-slip, manner, resulting in oscillations in the tear force. Stick-slip tear propagation has been observed previously in vulcanized rubber [20] and filled elastomers [21]. Greensmith et al. [20] attributed this phenomena in vulcanized rubber to a decrease in the tear energy with an increase in the rate of crack propagation.

Compared to elastomers, the thermoplastics used in FFF are viscoplastic materials that exhibit yield, post-yield softening, and hardening. Tearing may produce significant rate-dependent plastic dissipation that would add to the intrinsic tear energy. It is not clear how the features of the viscoplastic stress response, such as the post-yield stress drop and hardening modulus, affect the plastic dissipation, the stick-slip propagation behavior, and mode mixty. The FFF printed specimens are also thicker than elastomeric sheets typically used in tear tests. Davis et. al. [9] used a specimen with a thickness to the width ratio of 0.1. A thicker specimen produces higher bending stresses, which may lead to large plastic deformation in the tear arms. The elliptical cross-section of the printed filaments form grooves that could concentrate stresses at the weld surface leading to a more complicated mode mixty and larger plastic deformation ahead of the propagating tear. These factors, as well as the finite width of the tear specimens, may cause the plastic dissipation and the tear energy to depend on the specimen geometry.

In this work, we developed a finite element model of a tear test of an FFF printed wall to study the specimen rotation and stick-slip phenomena observed in experiments and the effects of viscoplasticity on the tear energy. The following section presents a brief summary of the tear test method and a detailed description of the finite element analysis of the tear test. The finite element model was based on the geometry of a representative FFF printed specimen. The model was applied to study the effects of viscoplasticity on the mode mixty, crack propagation, and tear energy, and the effects of specimen geometry on the specimen rotation and the tear energy.

2. Methods

2.1. Experimental Method

The specimens tested for this study were printed using a Lulzbot Taz 6 Fused Filament printer (Fargo, ND) [1] with a 0.5 mm diameter nozzle and a Polyetherimide (PEI) build plate. The environmental chamber ([22]) was set to maintain an ambient temperature of 70 ^{o}C and relative humidity less than 15% RH. Stock filaments of clear polycarbonate with a diameter of 2.85mm were purchased from Ultimaker (Utrecht, The Netherlands) and dried at 140 ^{o}C for 1 hour prior to printing. A temperature sweep in a dynamical mechanical analyzer (DMA) revealed the glass transition temperature of the polycarbonate to be 129.5 ^{o}C. The Molecular weight was measured to be 25.0x103 with a PDI of 1.4 as measured with Static Light Scattering (SLS). Single-road wide hollow boxes, 100 mm on a side and 12 mm high, were printed and sectioned to make 80 mm long specimens (one road thick and 12 mm high) from each face

[1] Certain commercial equipment, instruments, or materials are identified in thispaper in order to specify the experimental procedure adequately. Such identificationis not intended to imply recommendation or endorsement by the National Institute of Standards and Technology, nor is it intended to imply that the materials orequipment identified are necessarily the best available for the purpose.

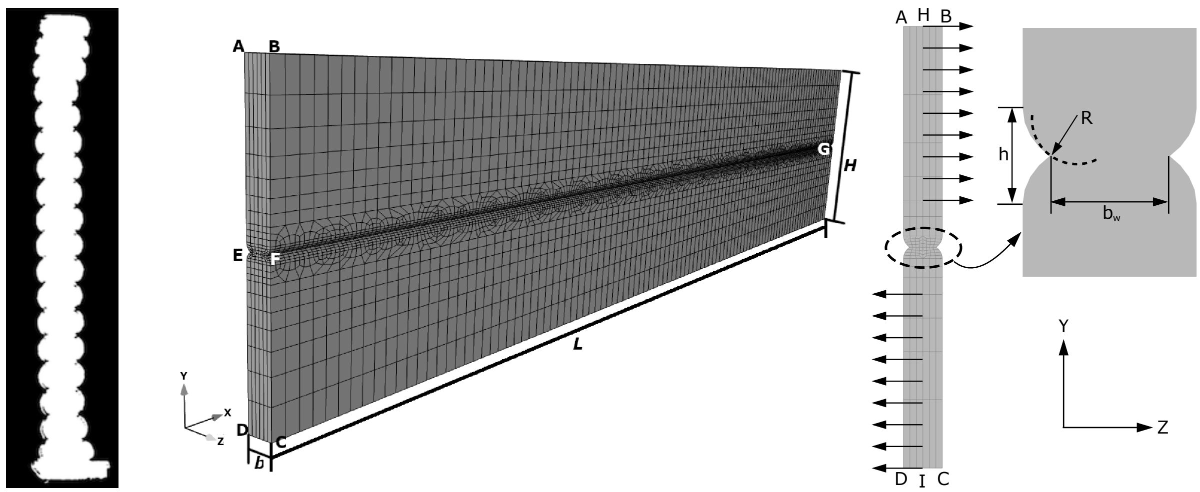

(a) (b) (c)

Figure 1: (a) The micro-CT image of a printed wall used for the tear test and (b) the 3D view and (c) side view of the finite element model of the specimen used for the tear simulations

.

of the box. The mode III tear tests were conducted on an MTS Criterion series 40 load frame (Eden Prairie, MN) equipped with an inline 100 N S-beam load cell with a sensitivity of 1.96 mV/V. A razorblade was used to cut the centermost weld at one end of each specimen. These cuts were extended by hand until they reached a nominal length of 20 mm. The cut ends of each sample were secured in flat grips and the upper grip was pulled up at a constant displacement rate of 1 mm/s, causing the crack to extend perpendicularly to the loading direction at 0.5 mm/s. The geometry of representative specimens was characterized using micro-Computed Tomography (μ-CT) on an EasyTom 150/160 (RX-Solutions, Plymouth, MN) and reconstructed using the Xact 64 software. The reconstructed slices with a voxel size of 7.6 μm were imported into MATLAB R2018b and characterized with its Image Processing Toolbox; the bond width and the shape of the extruded layers were obtained for various print parameters. A representative μ-CT slice is shown in Fig. Fig. 1(a). And more details on the printing, testing and characterization of these specimens can be found in the companion paper ([18]).

2.2. *Finite Element Model*

2.2.1. *Geometry and boundary conditions*

The finite element model (FEM) was based on the geometry of a representative FFF printed tear test specimen described in Sec. 2.1. The micro-computed tomography (μ-CT) image of the specimen cross-section (Fig. 1a) showed that the elliptical shape of the filaments created a scalloped structure (Fig. 1b, c). The grooves formed by the scallops may concentrate stresses at the weld and it was important to represent the elliptical shape of the filament cross section at the crack plane in the finite element model. However, to reduce the number of elements and make the computation more tractable, a uniform thickness was assumed for the rest of the specimen. The result was a grooved flat sheet with the groove height h, wall height H, length L, width b, and bond width b_w. The groove was represented by two overlapping ellipses. The radius of curvature R of the ellipse as measured at the intersection point can be calculated from h, b, and b_w as,

$$R = \frac{\sqrt{b^2 - b_w^2}}{2hb^2}\left(\frac{h^2 b_w^2}{b^2 - b_w^2} + b^2 - b_w^2\right)^{1.5} \tag{1}$$

The dimensions of the model were varied as shown in Table. 1 to investigate the effects of the specimen geometry on the crack propagation and tear energy. The parameters H, h, b, and b_w of the baseline geometry were obtained from the OCT image shown in FIg. 1a. The length $L = 30$ mm was chosen for all the cases to be long enough to obtain steady-state crack propagation.

The baseline geometry was discretized using an unstructured mesh of 33084 trilinear hexagonal elements. The mesh size was biased to achieve a finer mesh towards the weld plane. The surface labeled EFG in Fig. 1c was discretized using a uniform structured mesh of 8×300 bilinear quadrilateral cohesive surface elements (CSE), which prescribed a traction-separation law between the surfaces. Part of the CSEs were disabled to create initially separated surfaces to represent the pre-crack in the experiments. Finite element analysis was performed using Tahoe[2], which is an open source finite element program.

Displacement boundary conditions were applied on the midline HI of the front surface ABCD (Fig. 1c) to produce tearing. The displacement in the Y and X directions were fixed at zero, while the Z component of the displacement was $D_Z = Vt$ on bottom section and $D_Z = -Vt$ on the top section, where V is the applied velocity and t is the time. The other surfaces of the specimen were set to be traction free.

Table 1: Geometric dimensions for the parametric study, the dimensions were given in mm

Case	H	b	b_w	R	h
Baseline	6	0.5322	0.36772	0.2498	0.2922
A	3	0.5322	0.36772	0.2498	0.2922
B	4.6	0.5322	0.36772	0.2498	0.2922
C	10	0.5322	0.36772	0.2498	0.2922
D	6	0.2	0.2	inf	NA
E	6	0.2	0.3	inf	NA
F	6	0.4	0.4	inf	NA
G	6	0.5322	0.3	0.2987	0.2922
H	6	0.5322	0.44	0.2595	0.2922
I	6	0.5322	0.5322	inf	NA

2.2.2. *Constitutive model for the polycarbonate*

A viscoplastic model was applied to capture the rate-dependent yield and post-yield behavior of polycarbonate at room temperature. To model the viscoplastic behavior, the deformation gradient was assumed to be decomposed multiplicatively into an elastic and viscous part, $\mathbf{F} = \mathbf{F}_e\mathbf{F}_v$. The Helmholtz free energy density was assumed to be composed of a contribution Ψ_N from the long-range network interactions dependent on the Cauchy-Green tensor $\mathbf{C} = \mathbf{F}^T\mathbf{F}$ and a contribution Ψ_I from the short-range intermolecular interactions dependent on elastic right Cauchy-Green tensor $\mathbf{C}_e = \mathbf{F}_e^T\mathbf{F}_e$,

$$\Psi = \Psi_N(\mathbf{C}) + \Psi_I(\mathbf{C}_e), \tag{2}$$

A Neo-Hookean model was applied to describe the deviatoric response for both contributions of the free-energy density, and the Ogden model was applied to describe the equilibrium volumetric response as shown below,

$$\begin{aligned} \Psi_N &= \frac{1}{2}\mu_N\left(\mathrm{tr}(\bar{\mathbf{C}}) - 3\right) + \frac{1}{4}\kappa\left(J^2 - 1 - 2\ln J\right), \\ \Psi_I &= \frac{1}{2}\mu_I\left(\mathrm{tr}(\bar{\mathbf{C}}_e - 3\right), \end{aligned} \tag{3}$$

where $\bar{\mathbf{C}} = \det(\mathbf{C})^{-1/3}\,\mathbf{C}$ and $\bar{\mathbf{C}}_e = \det(\mathbf{C}_e)^{-1/3}\,\mathbf{C}_e$ are the deviatoric part of $\mathbf{C}$ and $\mathbf{C}_e$ respectively, and $J = \det(\mathbf{C})^{1/2}$ is the volumetric deformation. The second Piola-Kirchhoff stress is defined from the nonlinear viscoelasticity theory as [23],

$$\mathbf{S} = 2\frac{\partial\Psi}{\partial\mathbf{C}} = 2\frac{\partial\Psi_N}{\partial\mathbf{C}} + \mathbf{F}_v^{-1}\cdot 2\frac{\partial\Psi_I}{\partial\mathbf{C}_e}\cdot\mathbf{F}_v^{-T}, \tag{4}$$

[2] https://sourceforge.net/projects/tahoe/

and the Cauchy stress σ can be calculated as,

$$\sigma = J^{-1}\mathbf{F}\mathbf{S}\mathbf{F}^{T} = \frac{1}{J}\mu_N\left(\bar{\mathbf{b}} - \mathbf{I}\right) + \frac{1}{J}\mu_I\left(\bar{\mathbf{b}}_e - \mathbf{I}\right) + \frac{1}{2J}\kappa(J^2 - 1)\mathbf{I}. \tag{5}$$

The $\bar{\mathbf{b}}$ is the deviatoric part of the left Cauchy Green tensor $\mathbf{b} = \mathbf{F}\mathbf{F}^{T}$ and the $\bar{\mathbf{b}}_e$ is the deviatoric part of the elastic left Cauchy Green tensor $\mathbf{b}_e = \mathbf{F}_e\mathbf{F}_e^{T}$.

The following evolution law was used to determine the rate-dependent viscous deformation [23],

$$\frac{1}{2}\mathscr{L}_v\mathbf{b}_e = -\frac{1}{\eta}\bar{\tau}_I \cdot \mathbf{b}_e \tag{6}$$

where $\mathscr{L}_v$ is the Lie derivative and an objective rate of $\mathbf{b}_e$, $\mathscr{L}_v\mathbf{b}_e = 2\mathbf{F}\cdot\overline{\mathbf{F}^{-1}\dot{\mathbf{b}}_e\mathbf{F}^{-T}}\cdot\mathbf{F}^{T}$, and $\bar{\tau}_I = 2\mathbf{F}_e \cdot \frac{\partial\Psi_{NEQ}}{\partial\mathbf{C}_e}\cdot\mathbf{F}_e^{T}$ is the deviatoric part of the non-equilibrium Kirchhoff stress tensor. The parameter η is the viscosity that describes the resistance to viscous flow. An Eyring model was applied to describe the stress-activated yield behavior exhibited by glassy polymers [24, 25],

$$\eta = \eta_0 \exp\left(\frac{s}{s_y}\right), \quad s = \sqrt{\frac{1}{2}\tau_I : \tau_I}. \tag{7}$$

The following evolution law was applied for the activation stress s_y to capture the post-yield dynamic softening behavior,

$$\dot{s_y} = H_s\left(1 - \frac{s_y}{s_{y\infty}}\right)\frac{s}{\eta}, \quad s_y(0) = s_{y0}, \tag{8}$$

where H_s is the softening modulus, s_{y0} is the initial activation stress, and $s_{y\infty}$ is the softened activation stress. The model contains 7 parameters in total. The Young's modulus $E = 1710$ MPa was determined from uniaxial compression tests of the polycarbonate printing material (Sec. 2.1) as described in a prior study [26] and the Poisson's ratio was assumed to be $\nu = 0.35$. The parameters of the bulk modulus and shear modulus were determined from the measured Young's modulus and assumed Poisson's ratio, as, κ = 2000 MPa and $\mu_N + \mu_I$ = 630 MPa. The μ_N represents the resistance to network deformation during plastic deformation and determines the post-yield hardening modulus. The intrinsic viscosity η_0 and the initial value of the activation stress s_{y0} were fit to the yield stress at different strain rates as described in Wang et al. [26]. The softening parameter H_s was fit to the post-yield softening response and $s_{y\infty}$ was fit to the draw stress, which is the minimum stress in the post-yield stress response. A summary of the material parameters is given in Table 2. Figure 2 shows the stress response for the parameters in Table 2 for different strain rates. The parameters of the post-yield stress drop and the hardening modulus μ_N were varied as shown in Table 3 for the parameter study to investigate the effects on the tear strength and crack propagation.

Table 2: Summary of the baseline material parameters

Parameter	Physical significance	Values
κ	Bulk modulus	2000 MPa
μ_N	Equilibrium shear modulus, also hardening shear modulus	4 MPa
μ_I	Nonequilibrium shear modulus	626 MPa
η_0	Reference viscosity	6500 MPa·s
s_{y0}	Initial yield stress	55 MPa
$s_{y\infty}$	Steady state yield stress	33 MPa
H_s	Post-yield softening modulus	800 MPa

2.2.3. Constitutive model for the cohesive zone elements

In our tear experimental study [18], we examined the fracture surface of the printed polycarbonate specimens after the tear tests. The fracture surfaces for layer height and printing parameters described in Sec. 2.1 appeared smooth and did not show signs of crazing. Thus, we assumed that weld was inherently brittle and used the Xu-Needleman model

Table 3: Material parameters for the parametric study

Case	μ_N	μ_I	s_{y0}	$s_{y\infty}$
Baseline	4	626	55	33
1	8	622	55	31.45
2	12	618	55	30.1
3	24	606	55	36.84
4	4	626	65	32.84
5	4	626	45	33.28
6	4	626	35.5	34.43
7	4	626	55	55
8	4	626	33	33

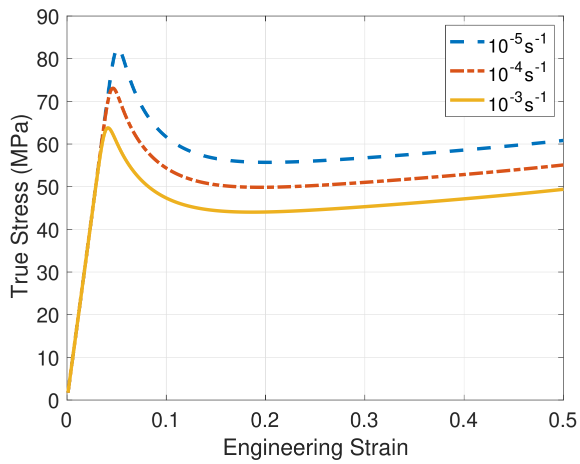

Figure 2: The strain-stress curve of the baseline material parameters in the uniaxial compression simulation under engineering strain rates from $10^{-3}/s$ to $10^{-5}/s$

[27] to describe the traction-separation relations of the CSEs. The Xu-Needleman model postulates the following potential for the cohesive energy Φ that depends on the normal separation Δ_n and tangential separations Δ_{t_1} and Δ_{t_2}:

$$\Phi(\Delta_n, \Delta_{t_1}, \Delta_{t_2}) = \Phi_n + \Phi_n \exp\left(-\frac{\Delta_n}{\delta_n}\right)\left[\left(1 - r + \frac{\Delta_n}{\delta_n}\right)\frac{1-q}{r-1} - \exp\left(-\frac{\Delta_{t_1}^2 + \Delta_{t_2}^2}{\delta_t^2}\right)\left(q + \frac{r-q}{r-1}\frac{\Delta_n}{\delta_n}\right)\right] \tag{9}$$

The normal and tangential tractions are defined as,

$$\begin{aligned} T_n &= \frac{\partial \Phi}{\partial \Delta_n} = \frac{\Phi_n}{\delta_n}\exp\left(-\frac{\Delta_n}{\delta_n}\right)\left[\frac{\Delta_n}{\delta_n}\exp\left(-\frac{\Delta_{t_1}^2 + \Delta_{t_2}^2}{\delta_t^2}\right) + \frac{1-q}{r-1}\left(1 - \exp\left(-\frac{\Delta_{t_1}^2 + \Delta_{t_2}^2}{\delta_t^2}\right)\right)\left(r - \frac{\Delta_n}{\delta_n}\right)\right] \\ T_{t_1} &= \frac{\partial \Phi}{\partial \Delta_{t1}} = 2\frac{\Phi_n}{\delta_t}\frac{\Delta_{t_1}}{\delta_t}\left(q + \frac{r-q}{r-1}\frac{\Delta_n}{\delta_n}\right)\exp\left(-\frac{\Delta_n}{\delta_n}\right)\exp\left(-\frac{\Delta_{t_1}^2 + \Delta_{t_2}^2}{\delta_t^2}\right) \\ T_{t_2} &= \frac{\partial \Phi}{\partial \Delta_{t2}} = 2\frac{\Phi_n}{\delta_t}\frac{\Delta_{t_2}}{\delta_t}\left(q + \frac{r-q}{r-1}\frac{\Delta_n}{\delta_n}\right)\exp\left(-\frac{\Delta_n}{\delta_n}\right)\exp\left(-\frac{\Delta_{t_1}^2 + \Delta_{t_2}^2}{\delta_t^2}\right) \end{aligned} \tag{10}$$

The readers are referred to the work by Xu and Needleman[27] for a detailed derivation of the model. The Xu-Needleman model is characterized by 5 parameters: the normal cohesive energy Φ_n, the characteristic normal separation δ_n, the characteristic tangential separation δ_t, the ratio of the tangential cohesive energy to the normal cohesive

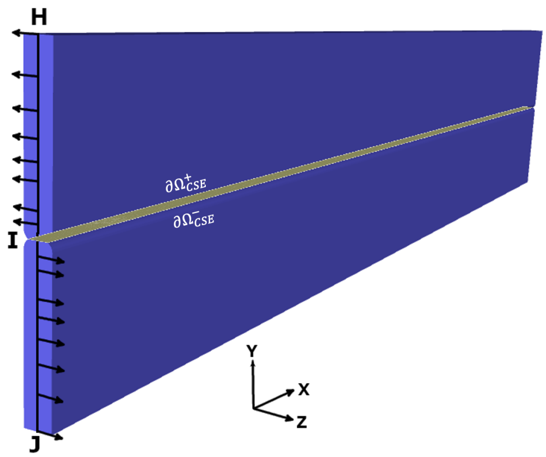

Figure 3: The diagram for the energy balance of the tear test

energy q, and the normal opening after pure shear separation r. For simplicity, we set $r = 0$ and $q = 1$ so that the tangential and normal cohesive energies are the same. The $\Phi_n = 8$ kJ/m^2 was fit to the steady-state tear force measured in experiments for the baseline geometry. Both the maximum normal and tangential tractions of the cohesive zone were assumed to be 50 MPa, which was the draw stress exhibited in uniaxial compression stress-strain curves, after post-yield softening and before hardening [26]. The maximum tractions were used to calculate characteristic separation parameters δ_n and δ_t from Φ.

2.2.4. Energy analysis of the tear test

The contribution of the viscoplastic dissipation and cohesive energy to the tear force during the steady-state tearing can be determined from an energy analysis of the tear geometry shown Fig. 1c. The balance of power can be written for a general mechanical system as,

$$\underbrace{\int_{\partial\Omega_0} \mathbf{T}\cdot\mathbf{V}dS}_{P_{ext}} = \underbrace{\int_{\Omega_0} \mathbf{S} : \frac{1}{2}\dot{\mathbf{C}}dV}_{P_{int}}. \tag{11}$$

The left hand side of the above equation is the external power P_{ext} caused by the traction $\mathbf{T}$ acting on the external surfaces and cohesive surfaces of the specimen deforming with a material velocity, $\mathbf{V}$. The right hand side is the internal power P_{int}, where $\mathbf{S}$ is the second Piola-Kirchhoff stress and $\dot{\mathbf{C}}$ is the material deformation rate.

The traction is zero on all surfaces except on the crack plane $\partial\Omega_{CSE}$, where the traction is the cohesive traction, and on the line HI, where the displacements are uniformly applied along the two sections HI and IJ in the z direction (Fig. 3). Denoting the resultant force and applied uniform displacement rate (i.e., velocity) acting on the section JI as F_z and V_z, respectively, and likewise on the section HJ as $-F_z$ and $-V_z$, the external power can be evaluated as,

$$\begin{aligned}
P_{ext} &= F_zV_z + (-F_z)(-V_z) + \int_{\partial\Omega^+_{CSE}} \mathbf{T}^+\cdot\frac{1}{2}\dot{\mathbf{\Delta}}dS + \int_{\partial\Omega^-_{CSE}} \mathbf{T}^-\cdot\frac{1}{2}\dot{\mathbf{\Delta}}dS \\
&= 2F_zV_z - \int_{\partial\Omega^+_{CSE}} \frac{\partial\Phi}{\partial\mathbf{\Delta}}\cdot\dot{\mathbf{\Delta}}dS \\
&= 2F_zV_z - \frac{\partial}{\partial t}\int_{\partial\Omega^+_{CSE}} \Phi dS \\
&= 2F_zV_z - \Phi_n b_w v_a,
\end{aligned} \tag{12}$$

where v_a is the crack propagation velocity.

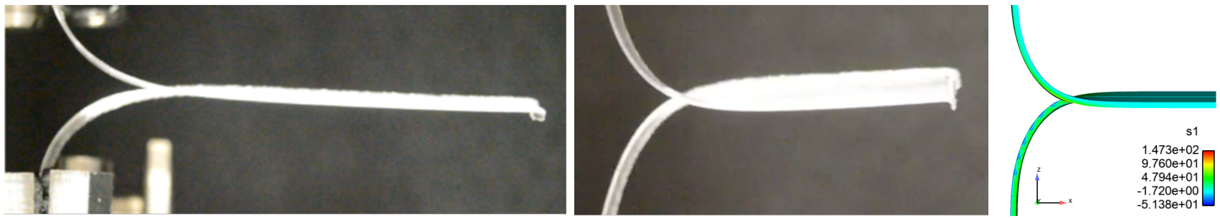

(a) (b) (c)

Figure 4: Images of the specimen (a) at the beginning of the tear test and (b) during the tear test showing specimen rotation opposite to the direction applied by the tear arms. (c) Contours of the maximum principal stress (in MPa) showing the same specimen rotation direction as in experiments. The front tear arm was pulled upwards and the back tear arm was pulled downward, which should generate a rotation in the $-x$ direction. However, the specimen ahead of the crack tip rotated in the $+x$ direction.

The internal power P_{int} can be evaluated by applying eq. (4) for the definition of $\mathbf{S}$ and the relation $\dot{\mathbf{C}} = \dot{\overline{\mathbf{F}_v^T \mathbf{C}_e \mathbf{F}_v}} = \dot{\mathbf{F}}_v^T \mathbf{C}_e \mathbf{F}_v + \mathbf{F}_v^T \dot{\mathbf{C}}_e \mathbf{F}_v + \mathbf{F}_v^T \mathbf{C}_e \dot{\mathbf{F}}_v$ to give,

$$P_{int} = \underbrace{\int_{\Omega_0} \left(\frac{\partial \Psi_N}{\partial \mathbf{C}} : \dot{\mathbf{C}} + \frac{\partial \Psi_I}{\partial \mathbf{C}_e} : \dot{\mathbf{C}}_e \right) dV}_{E} + \underbrace{\int_{\Omega_0} 2\mathbf{C}_e \frac{\partial \Psi_I}{\partial \mathbf{C}_e} : \dot{\mathbf{F}}_v \mathbf{F}_v^{-1} dV}_{D_{visc}} . \tag{13}$$

The $E = \int \dot{\Psi} dV$ is the rate of the stored free energy and D_{visc} is the rate of the dissipated energy from viscoplastic deformation. Combining eq.(11), (12) and (13), we arrive at the final normalized expression for the tear force,

$$\frac{2F_z}{\Phi_n b_w} = \frac{v_a}{V_y} + \frac{E}{V_y \Phi_n b_w} + \frac{D_{visc}}{V_y \Phi_n b_w}. \tag{14}$$

The first term in the right hand side represents the contribution from the cohesive energy, the second term in the right hand side is the normalized stored free energy, and the third term in the right hand side is the normalized viscoplastic dissipation energy. In the case of negligible inelastic deformation, D_{visc}=0, and steady crack propagation, $\frac{v_a}{V_y} = \frac{1}{\lambda}$, where λ is the stretch of the tear arm, eq. (14) reduces to the usual energy balance for the tear test [1],

$$2F_z \lambda = \Phi_n b_w + \frac{d \int \Psi dV}{da}. \tag{15}$$

3. Results and discussion

3.1. Specimen rotation during the tear test

In experiments, the specimen ahead of the crack tip was observed to rotate counter to the direction applied by the motion of the tear arms. In the top view (Fig.4), the front tear arm was pulled upwards and the back tear arm was pulled downwards, while the specimen ahead of the crack tip rotated in the opposite direction. The same phenomena was observed by Bayart et al. [19] in tear tests of polypropylene films. Fig.4(c) shows the side view of the deformed configuration for simulations of the baseline case. In the side view, the tear arms were pulled to create a rotation in the $-x$ direction, but the specimen ahead of the crack tip rotated in the $+x$ direction, which was the same as observed in experiments.

To understand the cause of this rotation, we simulated the tear test for different constitutive models and specimen geometries. Fig. 5(a) plots the rotation angle measured at the end of the specimen during the tear test using the viscoplastic model and the corresponding hyperelastic Neo-Hookean model. The bulk modulus and shear modulus of the Neo-Hookean model were set to be the same as the bulk modulus and the total shear modulus used in the viscoplastic model. The magnitude of the rotation angle increased monotonically and was nearly identical for the viscoplastic and hyperelastic models up to t = 725 s, which was the point of tear propagation in the hyperelastic

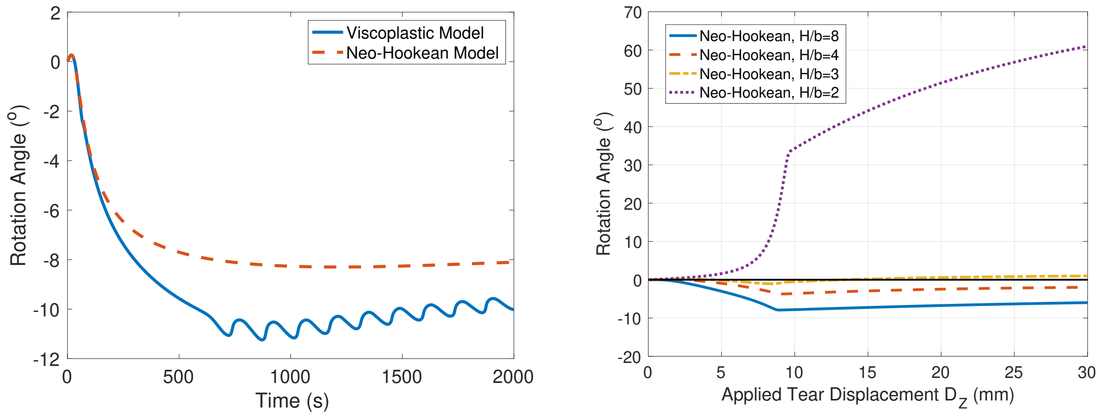

(a) (b)

Figure 5: Effects of material properties and specimen geometry on rotation during tearing:.(a) The viscoplastic and corresponding Neo-Hookean material models produced nearly identical rotations up the initiation of crack propagation. b)The rotation for different thickness to width H/b aspect ratios of the tear specimen, showing that H/b can be tailored to eliminate the effects of rotation. Case with positive angle rotates in the same direction as applied tear

model. Tear propagation in the viscoplastic model caused the rotation angle to start to oscillate, which corresponded to the stick-slip behavior discussed in the next section. The difference in the rotation angle between the two models was less than 30% and was caused by the difference in the initiation of tear propagation. Based on the small difference in the rotation angle before tear propagation, we conclude that the rotation was a result of the specimen geometry itself rather than the viscoplastic properties of the material.

We next applied the hyperelastic model to investigate the effects of the specimen geometry. A simpler geometry without a groove at the crack plane and smaller dimensions $L = 40$ mm and $b = b_w = 2$ mm, and a coarser mesh were used to reduce the computational cost. The specimen height H was varied to study its effects on the rotation angle (Fig. 5(b)) because H can be easily adjusted in experiments by changing the layer number. For a sheet-like geometry with a large aspect ratio ($H/b = 4, 8$), the specimen rotated in the direction counter to applied tear direction. The magnitude of the rotation angle for these thin sheets decreased slightly during tear propagation, which was consistent with the findings by Bayart et. al. [19]. For the intermediate case, where $H/b = 3$, the rotation of the specimen was close to zero. For the case with a small aspect ratio ($H/b = 2$), the specimen rotated in the same direction as the applied tear, and the magnitude of the rotation angle continued to increase during tear propagation. These results showed that for a given set of material properties, the aspect ratio of the tear specimen can be tailored to preclude specimen rotation during tear propagation.

3.2. Stick-slip tear propagation

At steady-state, the crack velocity v_a can be determined for the Xu-Needleman cohesive law as,

$$
\begin{aligned}
\Phi_n b_w v_a &= \int_{\partial\Omega^+_{CSE}} \dot{\Phi} dS, \\
v_a(t_n) &= \frac{1}{\Delta t}\left(\frac{1}{\Phi_n b_w}\int_{\partial\Omega^+_{CSE}} \Phi(t_n) dS - \frac{1}{\Phi_n b_w}\int_{\partial\Omega^+_{CSE}} \Phi(t_{n-1}) dS\right).
\end{aligned}
\tag{16}
$$

We applied v_a to approximate the crack velocity to investigate the development of stick-slip crack propagation. The tear force and v_a are plotted in Figure 6(b) for the finite element simulations. Before initiation, the tear force increased with increasing applied displacement of the tear arms. Crack propagation initiated at 61 s causing the crack velocity to jump to a finite value. As the crack propagated, the tear arms lengthened and the tear angle approached 90°, which resulted in a decrease in the tear force. Stick-slip crack propagation occurred at 625 s and was marked by oscillations

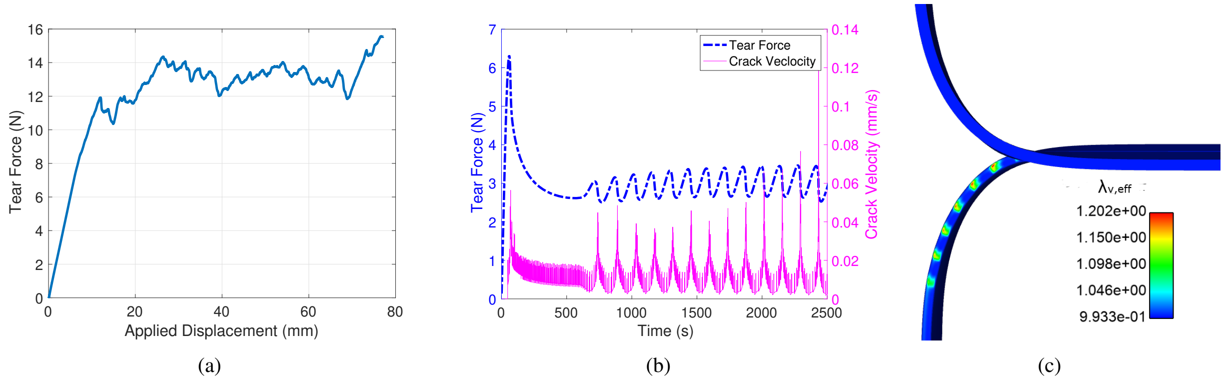

Figure 6: (a)Stick slip behavior is observed experimentally as oscillations in the tear force. (b) Both the tear force and the crack velocity started oscillating in the same period starting from time 625s due to the stick-slip behavior. (c) Contour of $\lambda_{\mathrm{v,eff}}$ shows a dot pattern on the crack plane, indicating the presence of plastic localization.

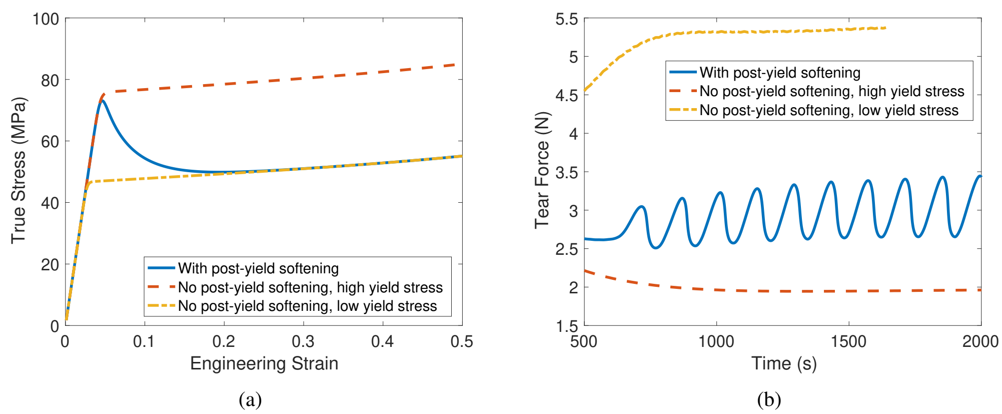

Figure 7: The tear test without post-yield softening shows no stick-slip behavior

in the tear force and crack velocity. The oscillations in the tear force and crack velocity were 90° out of phase. The tear force reached a maximum at zero velocity (stick) and a minimum when the velocity was maximum in the period (slip). The average tear force and the average v_a in a stick-slip period did not change significantly with crack propagation and thus was considered the steady-state tear force and crack velocity.

To investigate the contribution of plastic deformation to stick-slip tearing, we plotted the effective viscous stretch $\lambda^v_{eff} = \sqrt{\frac{1}{3}\left(\lambda_1^{v2} + \lambda_2^{v2} + \lambda_3^{v2}\right)}$ in Fig. 6(c), where λ_i^v is the principle viscous stretch. The plot shows a periodic pattern of plastic strain localization in the tear arms behind of the crack tip. The results showed that stick-slip propagation in the simulations occurred from plastic localization ahead of crack tip caused by the post-yield softening of the viscoplastic stress response. Plastic localization caused the crack to blunt rather than propagate. Continued plastic deformation led to strain hardening ahead of the crack tip, which allowed stresses to build up again in front of the crack tip to produce crack propagation. To test our hypothesis that plastic localization from post-yield softening caused the stick-slip behavior in the simulations, we simulated tearing of the same geometry using the same material parameters for the cohesive surfaces, but different parameters for the viscoplastic constitutive model to eliminate the post yield softening response (Fig. 7(a)). We further considered two cases (Case 7 and 8 in Tab. 3), where the yield stress was 0.96 and 1.5 times the maximum normal traction T_n of the cohesive surface to evaluate the effect of yield strength relative to the cohesive strength. The simulations without post-yield softening did not exhibit stick-slip tear

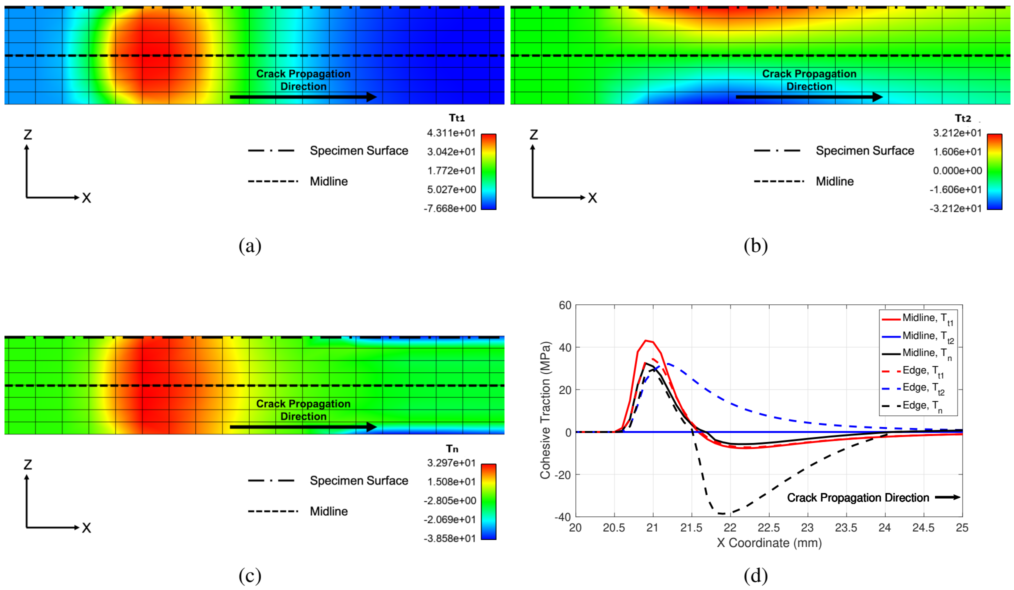

Figure 8: (a) The out-of-plane tangential traction, (b) in-plane tangential traction, and (c) normal traction are distributed non-uniformly on the crack plane near the crack-tip. (d) The cohesive tractions along the midline and the edge of the crack plane.

propagation. The tear force increased monotonically to a steady value for the low yield strength case and decreased to a lower steady-state value for the high-yield strength case (Fig. 7(b)). A lower yield strength promoted plastic deformation and blunting of the crack tip until the normal stress ahead of the crack tip exceeded the cohesive strength, which allowed the cohesive elements to separate and the crack to grow.

While the post-yield softening was the only source of the stick-slip propagation in the simulations, additional factors likely contributed to the stick-slip behavior in the experiments. These include variations in the bond width b_w, cross-section shape, weld strength, and molecular orientation along the printed filament. All of these factors could have produce the more irregular oscillations in the tear force and crack speed observed in experiments Fig. 6(a)

3.3. Cohesive tractions at the crack tip and the mode mixty

The linear elastic Mode III crack-tip stress field directly ahead of crack tip is given by:

$$\begin{aligned} \sigma_{yz} &= \frac{K_{III}}{\sqrt{2\pi r}} \\ \sigma_{xy} &= \sigma_{yy} = 0, \end{aligned} \tag{17}$$

where y is the direction normal to the crack plane, x is the crack propagation direction, r is the distance from the crack tip, and K_{III} is the mode III stress intensity factor. A notable feature of the Mode III crack tip stress field is that $\sigma_{xy} = \sigma_{yy} = 0$ ahead of the crack tip, and thus there are no normal and in-plane tangential tractions on the crack plane. Finite element simulations using the material properties listed in Tab. 3 for case 1 was applied to investigate the presence of mode mixty during tearing. Unlike the baseline case, case 1 did not exhibit stick-slip crack propagation, which may affect the crack tip stress field.

Fig. 8(a) plots the contour of the out-of-plane tangential traction T_{t1} on the crack plane, which corresponds to σ_{yz} in eq. 17. The red region in the contour is the crack-tip. The traction on the crack plane at the midline and at the specimen surface are plotted along the direction of crack propagation in Fig. 8(d). The T_{t1} was maximum at the midline of the crack plane and decreased symmetrically from the midline to the specimen surfaces on either side. The iso-stress lines for σ_{yz} formed a U-shape, which indicated that the crack front advanced further at the midline than

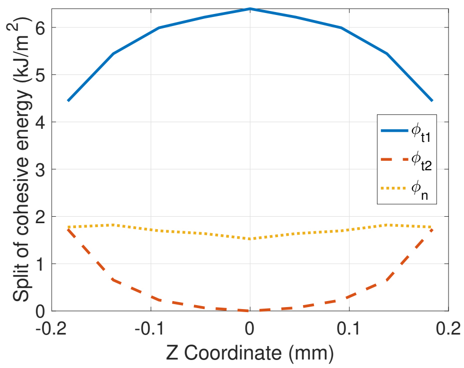

Figure 9: Cohesive work done by each component of the cohesive tractions at full separation in Case 6

at the specimen surface. Behind the crack tip, there was a region of negative T_{t1} that was around 6 times smaller in magnitude but distributed uniformly over the crack plane.

Fig. 8(b) plots the contour of the out-of-plane tangential traction T_{t2} on the crack plane, which corresponds to σ_{xy} in eq. 17. The traction T_{t2} varied asymmetrically across the midline of the crack plane. The value was zero at the midline, which was consistent with the linear elastic Mode III stress field. However, the magnitude of σ_{xy} were comparable to that of σ_{yz} at the specimen surfaces. The non-zero tangential traction T_{t2} on the specimen surfaces were caused by the bending of the tear arms in opposite directions, which resulted in tangential separation in the x direction.

Fig. 8(c) plots the contour of the normal traction T_n on the crack plane, which corresponds to σ_{yy} in eq. 17. Similar to σ_{yz}, σ_{yy} was maximum at the midline, varied symmetrically about the midline, and was negative ahead of the crack tip. However the normal stress increased to a large value at the specimen surface in front of the crack tip (Fig. 8(d)).

To quantitatively determine the mode mixty, the cohesive tractions were integrated with respect to the surface separation to obtain the cohesive work done by each component of the traction at full separation. The components of the cohesive energy can be evaluated as, $\phi_n = \int T_n \delta_n dt$, $\phi_{t1} = \int T_{t1}\delta_{t1}dt$, and $\phi_{t2} = \int T_{t2}\delta_{t2}dt$, where by definition $\phi_n + \phi_{t1} + \phi_{t2} = \Phi_n = 8\ kJ/m^2$ at full separation. The values were averaged along the crack propagation direction across the crack plane and plotted as a function of the their z coordinates. The $z = 0$ indicates the midline of the crack plane while $z = \pm 0.2$ indicates the two specimen surfaces. The work done by the out-of-plane shear tractions accounted for 80% of the cohesive energy at the midline and 55 % of the cohesive energy at the specimen surfaces, which suggested that tearing is primarily a mode III fracture problem. However, the work done by the normal tractions constituted around 20% of the cohesive energy and should not be neglected.

3.4. The effects of the material parameters

A parametric study was applied to investigate the effects of the hardening modulus and the peak stress on the tear energy. The parameters μ_N, μ_I, $s_{y\infty}$ were varied simultaneously to vary the hardening modulus and the peak stress while keeping the Young's modulus and the draw stress constant for the strain rate of 10^{-3} s^{-1}. The combinations of the material parameters are listed in the Table 3 and the strain-stress curves for uniaxial compression are shown in the Fig.10(a) and Fig. 11(a).

Cases 1-3 had the same peak stress and post-yield stress drop as the baseline case but a stiffer hardening modulus (Fig.10(a)). Increasing the hardening modulus μ_N eliminated stick-slip propagation and oscillations in the tear force (Fig.10(b)) by decreasing the strain range of the post-yield softening response. This allowed the material ahead of the crack tip to enter post-yield hardening regime shortly after post-yield softening.

Changing the hardening modulus had a modest effect on the tear energy and associated stored and dissipative energy components (Fig.10(c).) The tear energy was calculated using eq. 14, then averaged over a time window of 1500-2000 s, where the tear force and cohesive zone did not vary significantly with crack propagation. For the baseline case, the tear energy was calculated by averaging through the three stick-slip cycles in this time range. Increasing the hardening modulus μ_N from 4 MPa to 12 MPa increased the normalized tear energy by 10.8% from 2.06 to 2.31. Further increasing μ_N from 12 MPa to 24 MPa resulted in a slight 2.6% decrease in the normalized tear energy. For

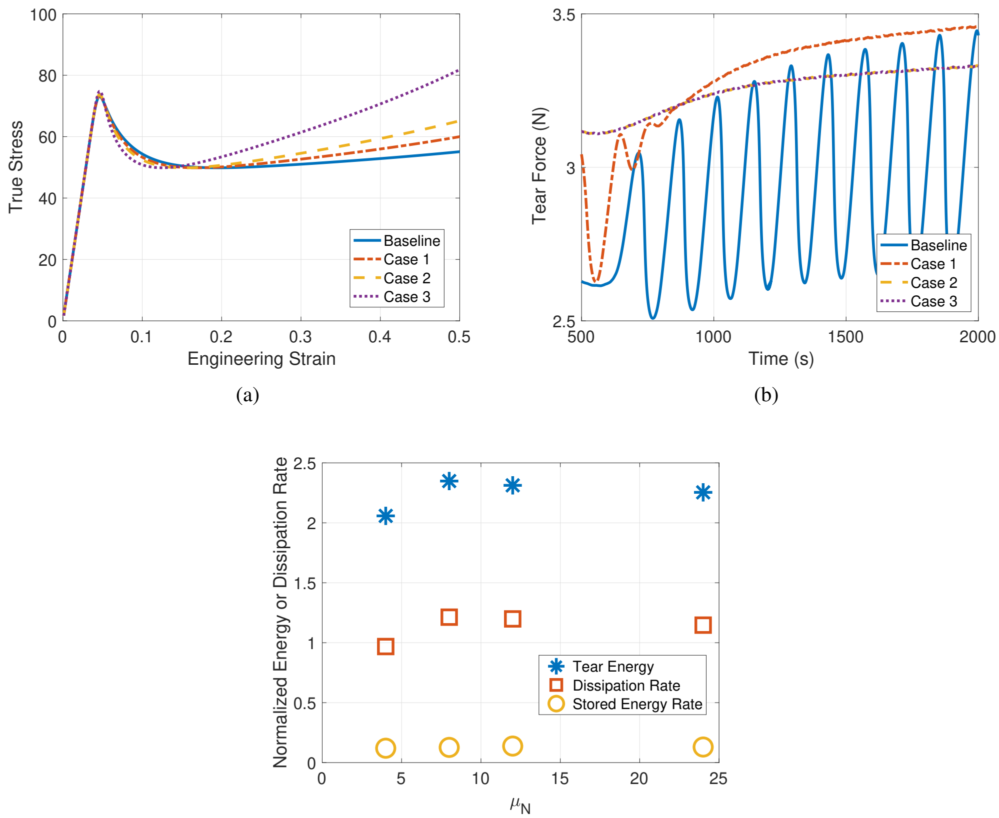

Figure 10: (a) The uniaxial compression strain-stress curves of parameters with different hardening modulus at the engineering strain rate of $10^{-3}s^{-1}$. (b) The tear forces versus time at (pseudo) steady state for materials with different hardening modulus. (c)The change in the hardening modulus has little influence on the tear energy and dissipation rate normalized by the cohesive energy per length $\Phi_n b_w$.

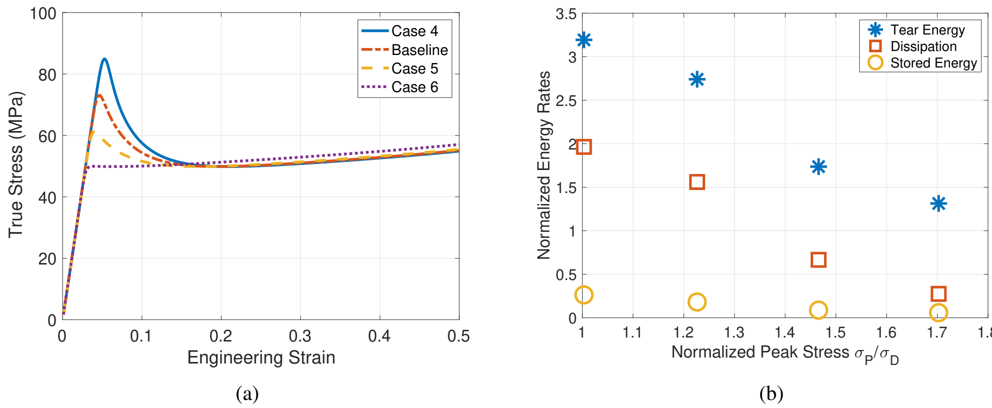

Figure 11: (a) The uniaxial compression strain-stress curves of parameters with different peak stress under the strain rate 10^{-3} s^{-1}. (b) The normalized tear energy and the normalized dissipation decreased with increasing peak stress, both are normalized by the cohesive energy per length $\Phi_n b_w$.

all cases, the normalized stored energy component was noticeably smaller than the tear energy. This was consistent with the small stretch (< 1.03) observed in the tear arms.

In contrast, changing the peak stress had a large effect on the tear energy. Increasing the peak stress relative to the cohesive strength from 1.0 to 1.7 decreased the normalized plastic dissipation energy by nearly a factor of 10 from 1.97 to 0.27. The normalized tear energy decreased by the same amount and became nearly 1.0, where the tear energy equal the cohesive energy. For glassy polymers, the peak stress and post-yield stress drop are increased by physical aging. These results indicate that physical aging would produce a more brittle fracture behavior for FFF printed materials.

3.5. The effects of the geometry on the tear energy

This section reports the effects of the geometry on the normalized tear energy and its stored and dissipative components. The baseline material and cohesive parameters were used for all cases, which produced stick-slip tear propagation and oscillations in the tear force. Thus, the tear energy, stored energy, and dissipative energy were averaged over 3 cycles of the tear force. The tear energy and the dissipation energy decreased significantly with the increasing specimen height H (Fig.12(a)). The normalized dissipation decreased by 88% when H increased from 3mm to 10mm. Decreasing the specimen height decreased the second moment of area, which increased the bending stress and produced greater plastic dissipation in the tear arms. A contour plot of the rate of plastic work (Fig.13) shows that the plastic zone was localized to the crack tip for the $H = 10$ mm case. In contrast the plastic zone spanned the tear arm for $H = 3$ mm.

Increasing the specimen width from $b = 0.2$ mm to $b = 0.53$ mm caused the normalized tear energy to increase from 1.64 to 3.74 and the normalized dissipation to increase more than four times from 0.58 to 2.55 (Fig.12(b)). In all three cases, the plastic zone was limited to a region of similar size around the crack tip (Fig. 14). However, the intensity of plastic work at the crack tip was greater for cases with larger width (Fig.14(b)). Increasing the bond width b_w from 0.3 mm to 0.5322 mm while maintaining the specimen width constant $b = 0.5322$ mm increased the normalized tear energy from 1.33 to 3.74 and increased the normalized dissipation from 0.56 to 2.55 (Fig.12(c)). A deeper groove produced a larger stress concentration and greater localization of the plastic deformation at the crack plane. This would inhibit crack blunting, decrease the plastic zone size and the plastic dissipation energy. Alternatively, a smaller bond width resulted in smaller surface energy per crack length, thus smaller tear force; while the bending moment remained the same because the layer width b was not changed. The smaller surface energy resulted in a less plastic bending and thus less dissipation. The simulation results were consistent with the experimental finding of Davis et al. [9] that the tear energy of a 3D printed wall with scalloped surfaces was smaller than the tear energy of the melt pressed films with flat surfaces. Experiments also show that the specimen would behave more ductile and the tear would be much harder to propagate if the scalloped structure were grounded flat. [OJ's experiment paper]

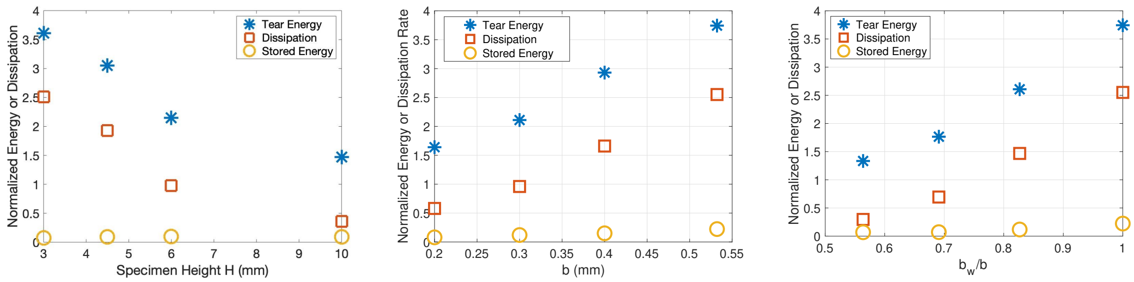

(a) (b) (c)

Figure 12: The normalized tear energy and the normalized dissipation rate (a) decreased with increasing specimen height H, (b) increased with increasing specimen width b, and (c) increased with the ratio of the bond width to the layer width

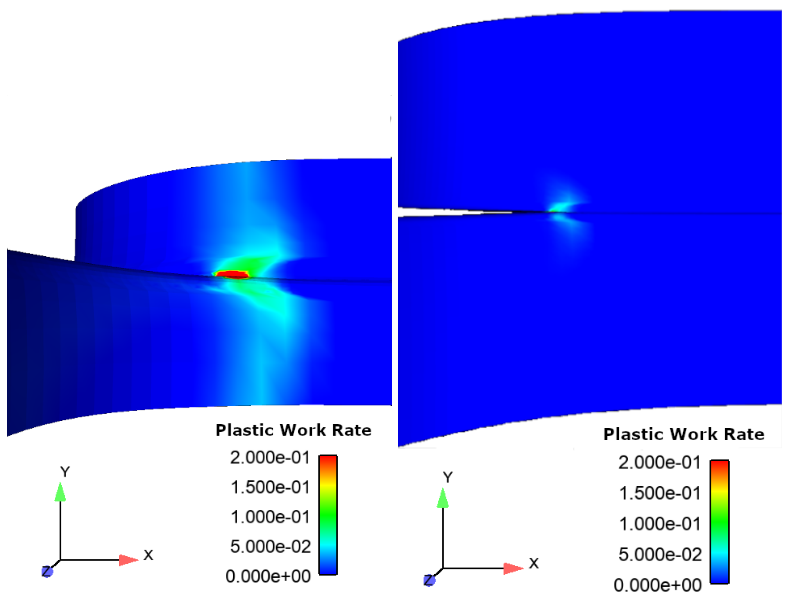

(a) (b)

Figure 13: The plastic zone size in the (a) H=3 mm case is larger than the (b) H=10 mm case

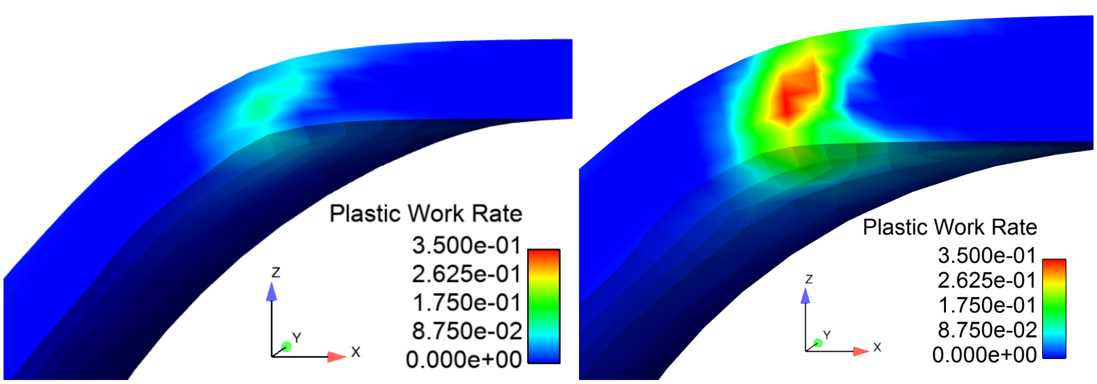

(a) (b)

Figure 14: The plastic work rate at crack tip in (a) b= 2mm case is smaller than (b) b=4 mm case

Numerous works have examined the effects of geometry on the tear energy for elastoplastic and viscoplastic materials. Isherwood et. al. [28] considered the tearing of thin sheets where the plastic zone was small compared to the height of the specimen. They calculated the tear energy for multiple materials, including aluminum foil, brass shim, and steel shim, and showed that the normalized tear energy decreased proportionally with decreasing specimen width b, which agreed well with the simulation results shown in Fig. 12(b). Mai et. al. [29] developed a theoretical model for the tear test of ductile metal sheets. They assumed uniform bending deformation across the height H of the specimen and applied a power-law strain-stress equation to analytically calculate the curvature of the tear arms and the total tear force. They found that the normalized tear energy increased with the specimen height H. Muscat-Fenech et. al. [30] considered a wider range of the specimen height and found that the normalized tear energy first increased then decreased with increasing specimen height as observed in the present study as shown in Fig. 12(a). The range of H considered in this study likely fell into the range of higher specimen height considered by Muscat-Fenech et. al. [30].

4. Conclusion

We applied finite element analysis to study the mechanics of the tear test for materials printed by a melt extrusion additive manufacturing process. The simulations were able to reproduce the stick-slip behavior and specimen rotation observed in experiments. The stick-slip behavior was found to be a result of strain localization caused by the post-yield softening behavior of glassy polymers. The magnitude and direction of the rotation was strongly influenced by the aspect ratio H/b of the specimen. For a given material, the aspect ratio can be tailored to eliminate specimen rotation. Analysis of the cohesive traction showed that tearing was predominantly Mode III at the middle of the crack plane. Away from the crack plane and towards the specimen surface, tearing became increasingly mixed between all three modes. At the specimen surface, Mode III, II and I contributed 55% and 25% and 20% respectively to the cohesive energy.

The tear energy increased with decreasing specimen height, increasing specimen width, and increasing ratio of the bond width to the specimen width. The increase was caused solely by increases in the plastic dissipation. The results showed that the plastic dissipation energy in the filament rather than the intrinsic cohesive energy of the weld can become the dominant contribution to the tear energy in a tear test. However, for a particular material properties, e.g., the peak stress and post-yield stress drop, the geometry of the tear specimen can be designed to minimize the effects of the bulk plastic dissipation. For sufficiently tall heights H, thin layer widths b, and a moderately small bond widths b_w that would not affect the intrinsic weld strength, the effect of plastic deformation can be localized to a small zone ahead of the crack tip such that the tear force would primarily measure the intrinsic cohesive energy of the weld.

References

[1] R. S. Rivlin, A. G. Thomas, Rupture of rubber. i. characteristic energy for tearing, Journal of Polymer Science 10 (3) (1953) 291–318. arXiv:https://onlinelibrary.wiley.com/doi/pdf/10.1002/pol.1953.120100303, doi:https://doi.org/10.1002/pol.1953.120100303.
URL https://onlinelibrary.wiley.com/doi/abs/10.1002/pol.1953.120100303

[2] A. D 1938-19, Standard test method for tear strength of conventional vulcanized rubber and thermoplastic elastomers, Tech. rep., ASTM International (2020).

[3] A. D 1938-19, Standard test method for tear-propagation resistance (trouser tear) of plastic film and thin sheeting by a single-tear method, Tech. rep., ASTM International (2019).

[4] C. Muscat-Fenech, J. Liu, A. Atkins, The trousers tearing test with ductile metal sheets, Journal of Materials Processing Technology 32 (1) (1992) 301 – 315. doi:https://doi.org/10.1016/0924-0136(92)90187-W.
URL http://www.sciencedirect.com/science/article/pii/092401369290187W

[5] H. Kimura, T. Masumoto, Fracture toughness of amorphous metals, Scripta Metallurgica 9 (3) (1975) 211 – 221. doi:https://doi.org/10.1016/0036-9748(75)90196-9.
URL http://www.sciencedirect.com/science/article/pii/0036974875901969

[6] M. V. Chin-Purcell, J. L. Lewis, Fracture of Articular Cartilage, Journal of Biomechanical Engineering 118 (4) (1996) 545–556. arXiv:https://asmedigitalcollection.asme.org/biomechanical/article-pdf/118/4/545/5543576/545_1.pdf, doi:10.1115/1.2796042.
URL https://doi.org/10.1115/1.2796042

[7] P. P. Purslow, Measurement of the fracture toughness of extensible connective tissues, Journal of Materials Science 18 (12) (1983) 3591–3598. doi:10.1007/BF00540731.
URL https://doi.org/10.1007/BF00540731

[8] K. Tonsomboon, C. T. Koh, M. L. Oyen, Time-dependent fracture toughness of cornea, Journal of the Mechanical Behavior of Biomedical Materials 34 (2014) 116 – 123. doi:https://doi.org/10.1016/j.jmbbm.2014.01.015.
URL http://www.sciencedirect.com/science/article/pii/S1751616114000162

[9] C. S. Davis, K. E. Hillgartner, S. H. Han, J. E. Seppala, Mechanical strength of welding zones produced by polymer extrusion additive manufacturing, Additive Manufacturing 16 (2017) 162 – 166. doi:https://doi.org/10.1016/j.addma.2017.06.006.
URL http://www.sciencedirect.com/science/article/pii/S2214860416303116

[10] M. Montero, S. Roundy, D. Odell, S.-H. Ahn, P. Wright, Material characterization of fused deposition modeling (fdm) abs by designed experiments, Proceedings of Rapid Prototyping and Manufacturing Conference (07 2001).

[11] N. G. Tanikella, B. Wittbrodt, J. M. Pearce, Tensile strength of commercial polymer materials for fused filament fabrication 3d printing, Additive Manufacturing 15 (2017) 40–47. doi:https://doi.org/10.1016/j.addma.2017.03.005.
URL https://www.sciencedirect.com/science/article/pii/S2214860416300859

[12] C. Koch, L. Van Hulle, N. Rudolph, Investigation of mechanical anisotropy of the fused filament fabrication process via customized tool path generation, Additive Manufacturing 16 (2017) 138–145. doi:https://doi.org/10.1016/j.addma.2017.06.003.
URL https://www.sciencedirect.com/science/article/pii/S2214860417300465

[13] E. A. Papon, A. Haque, Fracture toughness of additively manufactured carbon fiber reinforced composites, Additive Manufacturing 26 (2019) 41–52. doi:https://doi.org/10.1016/j.addma.2018.12.010.
URL https://www.sciencedirect.com/science/article/pii/S2214860418307371

[14] J. E. Seppala, S. Hoon Han, K. E. Hillgartner, C. S. Davis, K. B. Migler, Weld formation during material extrusion additive manufacturing, Soft Matter 13 (2017) 6761–6769. doi:10.1039/C7SM00950J.
URL http://dx.doi.org/10.1039/C7SM00950J

[15] N. A. Nguyen, C. C. Bowland, A. K. Naskar, A general method to improve 3d-printability and inter-layer adhesion in lignin-based composites, Applied Materials Today 12 (2018) 138–152. doi:https://doi.org/10.1016/j.apmt.2018.03.009.
URL https://www.sciencedirect.com/science/article/pii/S2352940718300933

[16] L. Fang, Y. Yan, O. Agarwal, J. E. Seppala, K. J. Hemker, S. H. Kang, Processing-structure-property relationships of bisphenol-a-polycarbonate samples prepared by fused filament fabrication, Additive Manufacturing 35 (2020) 101285. doi:https://doi.org/10.1016/j.addma.2020.101285.
URL https://www.sciencedirect.com/science/article/pii/S2214860420306576

[17] S. Charlon, J. Le Boterff, J. Soulestin, Fused filament fabrication of polypropylene: Influence of the bead temperature on adhesion and porosity, Additive Manufacturing 38 (2021) 101838. doi:https://doi.org/10.1016/j.addma.2021.101838.
URL https://www.sciencedirect.com/science/article/pii/S2214860421000038

[18] O. Agarwal, Z. Wang, S. H. Kang, J. E. Seppala, T. D. Nguyen, K. J. Hemker, Shape effect in the trouser tear test of a single weld formed by fff (In Preparation).

[19] E. Bayart, A. Boudaoud, M. Adda-Bedia, On the tearing of thin sheets, Engineering Fracture Mechanics 77 (11) (2010) 1849 – 1856, international Conference on Crack Paths 2009. doi:https://doi.org/10.1016/j.engfracmech.2010.03.006.
URL http://www.sciencedirect.com/science/article/pii/S0013794410001189

[20] H. W. Greensmith, A. G. Thomas, Rupture of rubber. iii. determination of tear properties, Journal of Polymer Science 18 (88) (1955) 189–200. arXiv:https://onlinelibrary.wiley.com/doi/pdf/10.1002/pol.1955.120188803, doi:https://doi.org/10.1002/pol.1955.120188803.
URL https://onlinelibrary.wiley.com/doi/abs/10.1002/pol.1955.120188803

[21] K. Sakulkaew, A. Thomas, J. Busfield, The effect of the rate of strain on tearing in rubber, Polymer Testing 30 (2) (2011) 163 – 172. doi:https://doi.org/10.1016/j.polymertesting.2010.11.014.
URL http://www.sciencedirect.com/science/article/pii/S0142941810001923

[22] L. Fang, Y. Yan, O. Agarwal, J. E. Seppala, K. J. Hemker, S. H. Kang, Processing-structure-property relationships of bisphenol-a-polycarbonate samples prepared by fused filament fabrication, Additive Manufacturing 35 (2020) 101285. doi:https://doi.org/10.1016/j.addma.2020.101285.
URL https://www.sciencedirect.com/science/article/pii/S2214860420306576

[23] S. Reese, S. Govindjee, A theory of finite viscoelasticity and numerical aspects, International Journal of Solids and Structures 35 (26) (1998) 3455 – 3482. doi:https://doi.org/10.1016/S0020-7683(97)00217-5.
URL http://www.sciencedirect.com/science/article/pii/S0020768397002175

[24] H. Eyring, Viscosity, plasticity, and diffusion as examples of absolute reaction rates, The Journal of Chemical Physics 4 (4) (1936) 283–291. arXiv:https://doi.org/10.1063/1.1749836, doi:10.1063/1.1749836.
URL https://doi.org/10.1063/1.1749836

[25] T. Ree, H. Eyring, Theory of non-newtonian flow. i. solid plastic system, Journal of Applied Physics 26 (7) (1955) 793–800. arXiv:https://doi.org/10.1063/1.1722098, doi:10.1063/1.1722098.
URL https://doi.org/10.1063/1.1722098

[26] Z. Wang, J. Guo, J. E. Seppala, T. D. Nguyen, Extending the effective temperature model to the large strain hardening behavior of glassy polymers, Journal of the Mechanics and Physics of Solids 146 (2021) 104175. doi:https://doi.org/10.1016/j.jmps.2020.104175.
URL https://www.sciencedirect.com/science/article/pii/S0022509620304051

[27] X.-P. Xu, A. Needleman, Numerical simulations of fast crack growth in brittle solids, Journal of the Mechanics and Physics of Solids 42 (9) (1994) 1397 – 1434. doi:https://doi.org/10.1016/0022-5096(94)90003-5.
URL http://www.sciencedirect.com/science/article/pii/0022509694900035

[28] D. Isherwood, J. Williams, Some observations on the tearing of ductile materials, Engineering Fracture Mechanics 10 (4) (1978) 887 – 895. doi:https://doi.org/10.1016/0013-7944(78)90042-5.
URL http://www.sciencedirect.com/science/article/pii/0013794478900425

[29] Y. W. Mai, B. Cotterell, The essential work of fracture for tearing of ductile metals, International Journal of Fracture 24 (3) (1984) 229–236. doi:10.1007/BF00032685.
URL https://doi.org/10.1007/BF00032685

[30] C. M. Muscat-Fenech, A. G. Atkins, Elastoplastic trouser tear testing of sheet materials, International Journal of Fracture 67 (1) (1994) 69–80. doi:10.1007/BF00032365.
URL https://doi.org/10.1007/BF00032365